

Chapter 2

DIGITAL HOLOGRAPHY AND MULTI-WAVELENGTH INTERFERENCE TECHNIQUES

Myung K. Kim, Lingfeng Yu, and Christopher J. Mann

Dept. of Physics, University of South Florida, Tampa, FL 33620

Abstract: Recent developments in digital holography techniques are presented. The Fourier transform and convolution methods to calculate the diffraction fields are compared with the angular spectrum method, which allows short reconstruction distances down to zero with flexibility in the control of image noise. Examples of applications of digital holography in biological microscopy are presented with submicron lateral resolution. The phase imaging digital holography using two wavelengths is described that achieves unambiguous phase unwrapping, even for noisy images common in biological imaging. The wavelength scanning digital interference holography (WSDIH) is described that allows tomographic imaging by numerical superposition of many holograms using a series of different wavelengths to synthesize short coherence length. The WSDIH technique is applied to image sub-surface structures of an animal tissue down to 1.5 mm depth with 10 μm axial resolution.

Key words: Computer holography; Tomography; Three-dimensional image acquisition; Phase contrast microscopy; Holographic interferometry.

1. INTRODUCTION

Dennis Gabor invented holography in 1948 while attempting to improve the resolution of electron microscopy. At the time however his invention could not be made practical, as there were no sources available with the required coherence. The invention of laser and the introduction of off-axis holography provided the critical elements to make holography a practical and powerful tool for large areas of applications from metrology, data storage, optical processing, device fabrication, and even fine arts. On the

other hand, the conventional process of holography using photographic plates is time-consuming and cumbersome. Real time process is not feasible unless one uses photorefractives and other nonlinear optical materials. Recently, the field of holography has been undergoing another paradigm shift by electronic image capture using CCD array cameras and digital processing of the holographic images[1,2,3].

By recording the phase as well as intensity of light wave, holography allows reconstruction of the images of three-dimensional objects, and gives rise to a host of metrological and optical processing techniques. With the advance of computer and electronic imaging technology, it is now very practical and often advantageous to replace portions of the holographic procedures with electronic processes. In digital holography, the holographic interference pattern is digitally sampled by CCD camera and the image is numerically reconstructed by applying the results from the diffraction theory. It offers a number of significant advantages such as the ability to acquire the images rapidly, the availability of both the amplitude and the phase information of the optical field and the versatility of the processing techniques that can be applied to the complex field data. The advances in digital imaging devices such as CCD and CMOS cameras and in computational and data storage capacities have been central to the widening applications of digital holography. In 1967, J. Goodman demonstrated the feasibility of numerical reconstruction of holographic images from a digitized vidicon image[4]. Schnars and Jueptner, in 1994, were the first to use a CCD camera connected to a computer as the input[1]. Since then, developments of digital holographic techniques and applications have been gaining pace ever more rapidly. Microscopic imaging by digital holography has been applied to imaging of microstructures[5,6] and biological systems[7,8,9,10]. In digital holography, the phase of the optical field, as well as the amplitude, results directly from the numerical diffraction of the optically recorded holographic interference pattern and leads to images of optical thickness profile with a precision of a fraction of a wavelength[11,12,13,14]. This can be utilized for numerical corrections of various aberrations of the optical system such as field curvature and anamorphism[15]. In microscopy applications[15], the reconstructed image can be numerically focused to any plane in the object. Although the common preconception is that most coherent imaging techniques such as holography has the degrading effect of coherent noise, through careful control of laser beam and other optical quality, remarkably clean images can be obtained. This is especially true with phase imaging digital holography because of its relative immunity to amplitude or phase noise of the laser profile. Numerous techniques have been developed to exploit the unique advantages of digital holography, such as the ability to reconstruct along any

inclined planes[16,17], to transmit holographic data over communication channels[18], and to even generate holograms of fluorescence patterns[19].

We present recent developments in digital holography techniques carried out in our laboratory. In Sec. 2, various methods to calculate the holographic diffraction fields are described and compared, and the effectiveness of the angular spectrum method is particularly emphasized. In Sec. 3, several examples of applications of digital holography in biological microscopy are presented. In Sec. 4, the phase imaging digital holography using two or more wavelengths is described that achieves unambiguous phase unwrapping by optical method. Section 5 describes the wavelength scanning digital interference holography that allows tomographic or optical section imaging by numerical superposition of many holograms using a series of different wavelengths to synthesize short coherence length. Section 6 gives concluding discussions and remarks.

2. DIGITAL HOLOGRAPHY PRINCIPLES

A common method for calculating the propagation of the optical field is based on the Fresnel diffraction theory. Let $E_0(x_0, y_0)$ be the two-dimensional pattern of the optical field on a plane. Then the field $E(x, y)$ at another plane a distance z away is given by

$$E(x, y) = E_0 \oplus S(x, y; z) \quad (2-1)$$

where the point spread function (PSF) is

$$S(x, y; z) = -\frac{ik}{2\pi z} \exp\left[ik\sqrt{x^2 + y^2 + z^2}\right]. \quad (2-2)$$

The convolution can be numerically calculated by three fast Fourier transforms, or the PSF can be simplified by the Fresnel approximation as

$$S(x, y; z) = -\frac{ik}{2\pi z} \exp\left[ikz + \frac{ik}{2z}(x^2 + y^2)\right], \quad (2-3)$$

which allows the calculation to be carried out as a single Fourier transform.

Suppose the object consists of a point source located at (X_o, Y_o) on the object plane (x_o, y_o) a distance z_o from the hologram plane H :

$$E_o(x_o, y_o) = \varepsilon_o \delta(x_o - X_o, y_o - Y_o). \quad (2-4)$$

The object field at the H plane is a spherical wave:

$$E_{ho}(x_h, y_h) = \varepsilon_o \exp \left\{ \frac{ik}{2z_o} \left[(x_h - X_o)^2 + (y_h - Y_o)^2 \right] \right\}. \quad (2-5)$$

The reference field at the H plane is a plane wave, incident at an angle from the z-axis:

$$E_{hr}(x_h, y_h) = \varepsilon_r \exp \left[i(k_x x_h + k_y y_h) \right] \quad (2-6)$$

where $k_x = \mathbf{k} \cdot \hat{\mathbf{x}}$ and $k_y = \mathbf{k} \cdot \hat{\mathbf{y}}$. The total field at the H plane is $E_h(x_h, y_h) = E_{ho} + E_{hr}$ and the intensity is:

$$\begin{aligned} I_h(x_h, y_h) &= |E_h|^2 \\ &= |\varepsilon_r|^2 + |\varepsilon_o|^2 \\ &\quad + \varepsilon_r \varepsilon_o^* \exp \left\{ -\frac{ik}{2z_o} \left[(x_h - X_o)^2 + (y_h - Y_o)^2 \right] + i(k_x x_h + k_y y_h) \right\} \\ &\quad + \varepsilon_r^* \varepsilon_o \exp \left\{ \frac{ik}{2z_o} \left[(x_h - X_o)^2 + (y_h - Y_o)^2 \right] - i(k_x x_h + k_y y_h) \right\} \end{aligned} \quad (2-7)$$

In digital holography, the intensity pattern is sampled at $(x_h, y_h) = \{(\alpha\Delta, \beta\Delta); \alpha, \beta = 0, 1, 2, \dots, N_x - 1\}$ by the CCD array of $N_x \times N_x$ pixels and effective size $a_x \times a_x$ with $a_x = N_x \Delta$:

$$\begin{aligned} I_h(\alpha, \beta) &= |\varepsilon_r|^2 + |\varepsilon_o|^2 \\ &\quad + \varepsilon_r \varepsilon_o^* \exp \left\{ -\frac{ik}{2z_o} \left[(\alpha\Delta - X_o)^2 + (\beta\Delta - Y_o)^2 \right] + i(\alpha k_x + \beta k_y) \Delta \right\} \\ &\quad + \varepsilon_r^* \varepsilon_o \exp \left\{ \frac{ik}{2z_o} \left[(\alpha\Delta - X_o)^2 + (\beta\Delta - Y_o)^2 \right] - i(\alpha k_x + \beta k_y) \Delta \right\} \end{aligned} \quad (2-8)$$

The first two terms are the zero-order terms due to the reference and object beams, which can be eliminated by a number of different methods. The use of phase-shifting digital holography removes the zero order and twin images through multi-exposure holographic recording while shifting the phase of reference field by an integer fraction of 2π [20,21]. Off-axis holography spatially separates the holographic images away from the undiffracted zero-order. One can also take separate exposures of reference and object waves and subtract these from the original holographic exposure, which is effective in reducing any noise from these terms. On the other hand, the off-axis configuration reduces the available spatial frequency bandwidth by half. The last two terms in (2-8) are the holographic twin images, and these can be separated if the off-axis angle of the reference beam is large enough. We take the third term as the holographic image term. Numerical reconstruction of the holographic image starts with a multiplication by a conjugate reference field:

$$\begin{aligned} H(\alpha, \beta) &\equiv I_h(\alpha, \beta) \cdot E_{hr}^*(\alpha, \beta) \\ &= |\varepsilon_r|^2 \varepsilon_o^* \exp \left\{ -\frac{ik}{2z_o} [(\alpha\Delta - X_o)^2 + (\beta\Delta - Y_o)^2] \right\} \end{aligned} \quad (2-9)$$

Numerical Fresnel diffraction is applied to this expression over a distance of z_i to obtain the holographic image over a grid of the same size and resolution as the CCD array $(x_i, y_i) = \{(\gamma\Delta, \delta\Delta); \gamma, \delta = 0, 1, 2, \dots, N_x - 1\}$:

$$\begin{aligned} E_i(\gamma, \delta) &= H \oplus S(\gamma, \delta; z_i) \\ &= -\frac{ik}{2\pi z_i} \exp(ikz_i) \\ &\quad \times \sum_{\alpha, \beta=0}^{N_x-1} \Delta^2 H(\alpha, \beta) \exp \left\{ \frac{ik\Delta^2}{2z_i} [(\alpha - \gamma)^2 + (\beta - \delta)^2] \right\} \end{aligned} \quad (2-10)$$

The image at $z_i = z_o$ is:

$$\begin{aligned}
E_i(\gamma, \delta) &= -\frac{ik\Delta^2}{2\pi z_i} |\varepsilon_r|^2 \varepsilon_o^* \exp(ikz_i) \\
&\quad \times \exp \left\{ \frac{ik}{2z_o} \left[(\gamma^2 \Delta^2 - X_o^2) + (\delta^2 \Delta^2 - Y_o^2) \right] \right\} \\
&\quad \times \sum_{\alpha, \beta=0}^{N_x-1} \exp \left\{ -\frac{ik\Delta}{z_o} \left[\alpha(\gamma\Delta - X_o) + \beta(\delta\Delta - Y_o) \right] \right\} \\
&= -\frac{ik\Delta^2}{2\pi z_i} |\varepsilon_r|^2 \varepsilon_o^* \exp(ikz_i) \\
&\quad \times \exp \left\{ \frac{ik}{2z_o} \left[(\gamma^2 \Delta^2 - X_o^2) + (\delta^2 \Delta^2 - Y_o^2) \right] \right\} \\
&\quad \times \exp \left\{ -\frac{ika_x}{2z_o} \left[(\gamma\Delta - X_o) + (\delta\Delta - Y_o) \right] \right\} \\
&\quad \times \frac{\sin \frac{ka_x}{2z_o} (\gamma\Delta - X_o) \sin \frac{ka_x}{2z_o} (\delta\Delta - Y_o)}{\sin \frac{k\Delta}{2z_o} (\gamma\Delta - X_o) \sin \frac{k\Delta}{2z_o} (\delta\Delta - Y_o)} \\
&\approx -\frac{ika_x^2}{2\pi z_i} |\varepsilon_r|^2 \varepsilon_o^* \exp(ikz_i) \delta_{\gamma, X_o/\Delta} \delta_{\delta, Y_o/\Delta}
\end{aligned} \tag{2-11}$$

The Kronecker delta in the last line follows from the $\sin N\theta / \sin \theta$ factors, familiar from the theory of diffraction by a grating. The ‘width’ of the Kronecker delta is $d_\gamma = \frac{2\lambda z_o}{N_x \Delta^2}$ pixels: i.e., d_γ pixels for $\frac{ka_x}{2z_o} (\gamma\Delta - X_o)$ to span $-\pi$ to $+\pi$. The discrete summation is in fact periodic and can lead to aliasing unless $\frac{k\Delta}{2z_o} (\gamma\Delta - X_o) < \pi$ for all γ , which is satisfied if

$$z_o > \frac{a_x^2}{N_x \lambda} = z_{\min} \tag{2-12}$$

This sets the minimum object-to-hologram distance, to avoid aliasing in the Fourier transforms.

The pixel resolution of the reconstructed images determined from the Fresnel diffraction formula as a single Fourier transform, varies as a function of the reconstruction distance z as $\Delta_1 = \lambda z / (N_x \Delta_0)$, where Δ_0 and Δ_1 are the resolutions of the hologram and the reconstructed image, respectively. In order to get consistent resolution, the Fresnel diffraction can also be implemented as a convolution, as described above. However, both of the above approaches assume the Fresnel approximation, which limits a minimum reconstruction distance z . By using the angular spectrum algorithm, the problems associated with the Fresnel diffraction formula are avoided. From Fourier optics[23], if $E(x, y; 0)$ is the object wave field at plane $z = 0$, the corresponding angular spectrum of the object wave at this plane is the Fourier transform:

$$F(k_x, k_y; 0) = \iint E(x, y; 0) \exp[-i(k_x x + k_y y)] dx dy, \quad (2-13)$$

where k_x and k_y are corresponding spatial frequencies of x and y . The object angular spectrum $F(k_x, k_y; 0)$ can be separated from other spectral components of the hologram with a numerical band-pass filter if the off-axis angle θ of the incident beam is properly adjusted. The object field $E(x, y; 0)$ can be rewritten as the inverse Fourier transform of its angular spectrum, properly filtered,

$$E(x, y; 0) = \iint F(k_x, k_y; 0) \exp[i(k_x x + k_y y)] dk_x dk_y. \quad (2-14)$$

The complex-exponential function $\exp[i(k_x x + k_y y)]$ may be regarded as a projection, on to the plane $z = 0$, of a plane-wave propagating with a wave vector (k_x, k_y, k_z) , where $k_z = [k^2 - k_x^2 - k_y^2]^{1/2}$ and $k = 2\pi/\lambda$. After propagating along the z axis to a new plane, the field distribution is

$$E(x, y; z) = \iint F(k_x, k_y; 0) \exp[i(k_x x + k_y y + k_z z)] dk_x dk_y. \quad (2-15)$$

This is the angular spectrum method and the resolution of the reconstructed images is the same as that in the hologram plane. In spite of the apparent differences, the angular spectrum method will yield identical predictions of diffracted field as the first Rayleigh-Sommerfeld solution[23]. However, as an approximate Rayleigh-Sommerfeld solution, Fresnel diffraction is not capable of reconstructing the wave field near to the hologram plane.

3. DIGITAL HOLOGRAPHIC MICROSCOPY EXPERIMENTS

The experiments are performed with modified Mach-Zhender interferometers, illustrated in Fig. 2-1. In reflective geometry (Fig. 2-1a), a collimated beam from the laser is split into the object and reference beams by the beam splitter BS1. The object beam is focused by the lens L2 on to the point F2, which is also the front focal point of the objective lens L3. Thus the object is illuminated by a collimated beam. An aperture A is placed at the conjugate point of the object with respect to L3, so that the aperture is imaged on the object and the illumination is confined to an area of the object that is being imaged by the holographic system. This is necessary to avoid light scattered from the surrounding area of the object entering the camera contributing to the noise of the imaging system. The laser light is reflected by the object and travels toward the camera, which is placed at the conjugate plane of the plane H with respect to L3. The reference beam's focus F1 is equidistant from BS3 as F2, so it is optically equivalent to a collimated beam incident from the left of objective L3. The object and the reference beams are tilted with respect to each other in an off-axis hologram arrangement. Figure 2-1b) illustrates another apparatus for transmissive geometry using a pulsed laser. A magnified image of an object specimen is projected on the CCD camera, as well as the reference beam. A pair of similar microscope objectives (L1 and L2) in the two optical branches are used to match the curvature of the two wavefronts. A digital delay generator (DDG) triggers both the laser and the camera.

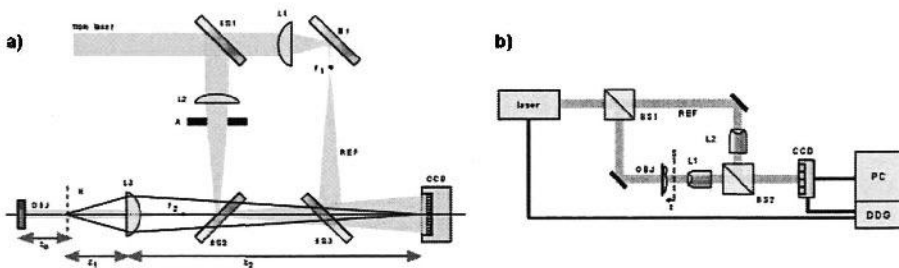


Figure 2-1. a) Apparatus for reflective digital holography. BS's: beam splitters and combiner; L's: lenses; F's: focal points; M1: mirror; A: aperture; OBJ: object; REF: reference; H: hologram plane, imaged to CCD plane; CCD: camera. b) Apparatus for transmissive digital holography. DDG: digital delay generator; PC: computer.

The digital holography experiment proceeds as follows, described using an example set of parameters. The wavelength is $\lambda = 0.532 \mu\text{m}$. An area of the object is chosen for imaging with $a_x = 88 \mu\text{m}$ and $N_x = 360$, so that $\Delta = 0.24 \mu\text{m}$. This gives $z_{\min} = 40 \mu\text{m}$, and z_o is set at this value. This area of H-plane is imaged by a microscope objective on to the CCD with lateral magnification $M = 37$, to correspond to the physical pixel size of $M\Delta = 9 \mu\text{m}$ and $Ma_x = 3.3 \text{ mm}$. The resolution of the imaging system given by Rayleigh criterion is $d = 1.22\lambda / 2N.A. = 0.82 \mu\text{m}$, using an $f = 8.55 \text{ mm}$ microscope objective lens with $N.A. = 0.4$. This corresponds to $Md = 30 \mu\text{m}$ at the CCD. On the other hand, the width of the PSF of the digital reconstruction is $d_y\Delta = 0.48 \mu\text{m}$, which again is smaller than the optical PSF d , and therefore the resolutions of the CCD array and the numerical reconstruction are all sufficient for the given optical system. The optical system described here provides a straightforward means for high resolution holographic microscopic imaging. There is no need for elaborate processing such as magnification by using reconstruction wavelength long compared to recording wavelength[3], which inevitably introduces aberration, or using an aperture array in front of the camera and scanning it to artificially increase the CCD resolution[22].

Figure 2-2 shows an $88 \times 88 \mu\text{m}^2$ area of a USAF resolution target. The element 6 of group 7 has $2.2 \mu\text{m}$ bar width, and the resolution of the image appears somewhat better than that, say $1 \mu\text{m}$. The holographic amplitude image, Fig. 2-2c), is quite indistinguishable from the direct image, Fig. 2-2a). Quantitative phase imaging is particularly effective in digital holography – one only needs to plot the phase of the calculated complex optical field, as shown in Fig. 2-2d). The thickness of the chrome coating on the glass plate of the resolution target is easily measured from the phase image to be about 75 nm .

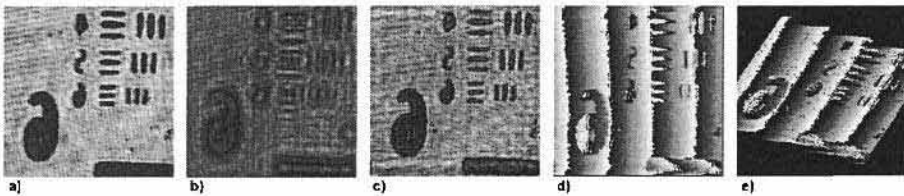


Figure 2-2. High resolution holographic image reconstruction of resolution target of area $88 \times 88 \mu\text{m}^2$ with 360×360 pixels. a) direct image when the object is on the H-plane, illuminated by laser; b) the hologram recorded by the camera; c) reconstructed amplitude image; d) phase image; e) phase image in perspective view.

The Fresnel transformation[7] has been commonly used to calculate the holographic diffraction, where the approximation of spherical Huygens

wavelet by a parabolic surface allows the calculation of diffraction integral using a single Fourier transform. In the Huygens convolution method[2], the diffraction integral can be calculated without such approximation using three Fourier transforms through the convolution theorem. On the other hand, the angular spectrum method[16] involves two Fourier transforms, plus simple filtering of the angular spectrum. We have applied all three methods to the reconstruction of the image of a resolution target, as shown in Fig. 2-3. A $25 \times 25 \mu\text{m}^2$ area of USAF resolution target is imaged containing the group 7 element 6 using 452×452 pixels. Figure 2-3a) is the holographic interference pattern recorded by the CCD camera, and its Fourier transform in Fig. 2-3b) is the angular spectrum. It contains three main peaks that correspond to the spectra of the zero-order and the two twin-images. One of these peaks – the highlighted rectangular area – is selected, a propagation phase factor is multiplied, and finally inverse-Fourier transformed to obtain the amplitude image in Fig. 2-3c) and the phase image in Fig. 2-3d). The individual bars are $2.2 \mu\text{m}$ wide, which are clearly resolved and consistent with diffraction-limited resolution of $0.5 \mu\text{m}$ for 0.65 NA lens. The physical thickness of film is given by $d = \lambda(\Delta\phi/2\pi)/(n-n_0)$, where λ is the wavelength, $\Delta\phi$ is the phase step, and $(n-n_0)$ is the index difference between the film and air. The thickness-equivalent noise level of the flat area is $\sim 30 \text{ nm}$. (On the film-coated opaque bar areas, the lack of light causes larger uncertainty in phase.) The phase map is rendered in pseudo-colored 3D perspective in Fig. 2-3i). Especially notable in the phase map is the lack of the coherent noise conspicuous in the amplitude image and prevalent in most other holographic imaging methods. The amplitude and phase images obtained from the Huygens convolution method are shown in Fig. 2-3e) and 2-3f), as well as those obtained from the Fresnel method in Fig. 2-3g) and 2-3h). The main reason for the obvious degradation of these images, calculated from the same hologram, is the insufficient off-axis angle to separate out the zero-order component. The effect is most detrimental in the Fresnel images, where part of the holographic image is buried in the zero-order background, and its phase image is completely scrambled. The effect shows up as the spurious interference patterns in the convolution images. While the minimum off-axis angle must be strictly satisfied in order to avoid the zero-order intrusion in Fresnel or convolution methods, the control and removal of zero-order component is straightforward and flexible in the angular spectrum method. Another potential problem of the Fresnel and convolution methods is that they require a minimum hologram distance to avoid aliasing, whereas the angular spectrum method does not have such minimum and the image can be calculated even at zero distance. The minimum distance is given by $z_{\min} = a^2/N\lambda$ where a is the size of the hologram and N is the number of pixels.

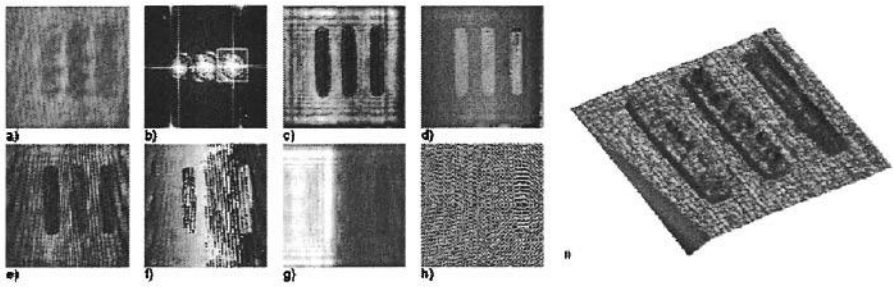


Figure 2-3. Holography of a resolution target.

Some examples of digital holography in biological microscopy are presented below. In Fig. 2-4, a $100 \times 100 \mu\text{m}^2$ area of a layer of onion cells is shown. The cell walls are sharply focused in the amplitude image and the phase image shows accurate representation of optical thickness, modulo wavelength, of the cell bodies. The phase-unwrapped image is generated using a software algorithm[24]. Figure 2-5 displays digital holography of a paramecium. Slightly different directions of reconstruction reference waves are used in the phase images c) and d), which may be useful for emphasizing different aspects of the microscopic images. Numerical focusing is another unique capability of digital holography, where a single hologram is used to calculate the optical field at any number of image planes, emulating the focusing control of a conventional microscope. In Fig. 2-6, a paramecium as well as a euglena (the thin rod shape in the upper right of the field) are within field of view but separated by about $400 \mu\text{m}$ of axial distance.

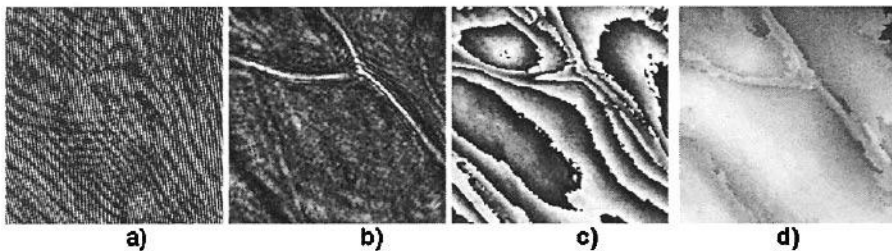


Figure 2-4. Holography of a layer of onion cells. Images, $100 \times 100 \mu\text{m}^2$, of a) hologram, b) amplitude, c) wrapped phase, and d) unwrapped phase.

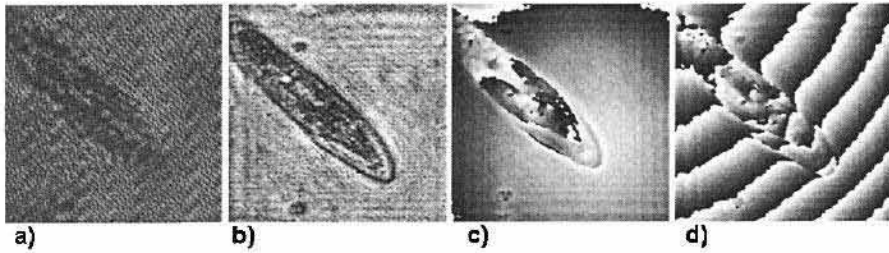


Figure 2-5. Holography of a paramecium, $250 \times 250 \mu\text{m}^2$, showing a) hologram, b) amplitude, c) and d) phase images.

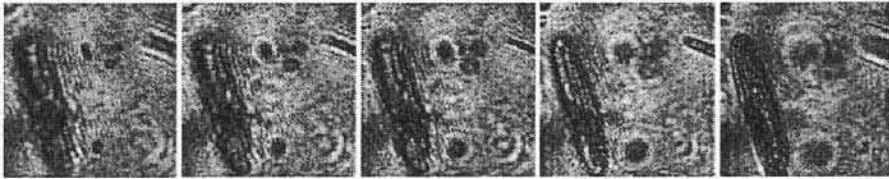


Figure 2-6. Numerical focusing in digital holography of paramecia.

We present two examples of high-resolution quantitative phase-contrast microscopy studies by angular spectrum digital holography. Figures 2-7 and 2-8 show images of SKOV-3 ovarian cancer cells: confluent group of cells in Fig. 2-7 and two isolated cells in Fig. 2-8. In each of the two cases, the panels display a) Zernike phase contrast image, b) holographic amplitude and c) phase images, and d) phase image unwrapped by a software algorithm. Pseudocolor 3D rendering of d) is shown in e). The image size is $60 \times 60 \mu\text{m}^2$ with 404×404 pixels. Figure 2-8 is a particularly good demonstration of the level of image resolution and fidelity that can be obtained by the present technique, displaying the nuclear membranes and chromosomes. The overall height of the cell is calculated to be about $2.8 \mu\text{m}$, with the assumption of the average index of the cell to be 1.375. Thickness of the lamellipodium around the edge of the cell is determined to be about 320 nm . The noise level in the substrate area is 60 nm , which may be partly due to the residues from fixing of the cells. These images represent a new level of capabilities in quantitative phase contrast imaging that is not available in current technology, in terms of the simplicity of principle and apparatus, quantitative accuracy of the representation, and versatility of processing techniques that can be applied.

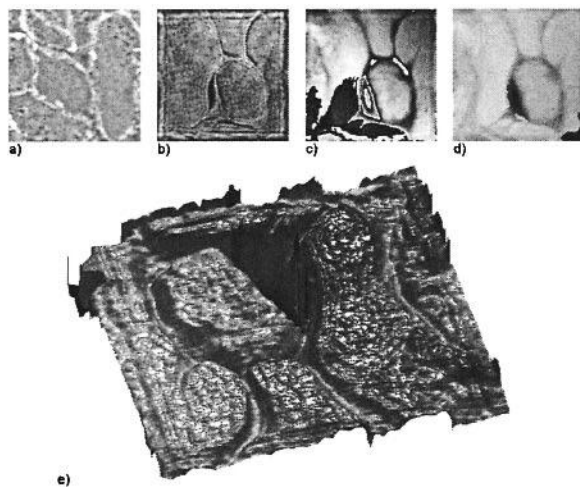


Figure 2-7. Holography of confluent SKOV-3 ovarian cancer cells. a) Zernike phase contrast image; b) holographic amplitude and c) phase images; d) unwrapped phase image; e) 3D pseudocolor rendering of d).

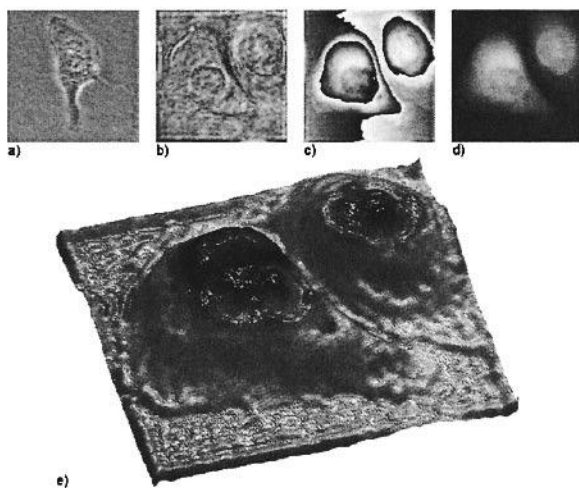


Figure 2-8. Holography of non-confluent SKOV-3 cells. a) Zernike phase contrast image; b) holographic amplitude and c) phase images; d) unwrapped phase image; e) 3D pseudocolor rendering of d).

4. MULTI-WAVELENGTH PHASE IMAGING DIGITAL HOLOGRAPHY

The digital holography is thus capable of high resolution microscopic imaging. In particular, the availability of the phase image can be of significant advantage with high precision of optical thickness profiles. On the other hand, the phase images contain 2π -discontinuities for objects of optical depth greater than the wavelength. Most of the phase unwrapping algorithms for removal of the discontinuities require subjective assumptions for detection of phase discontinuity when there are height steps on the object that are more than a wavelength[25,26]. The computation load is substantial at several minutes per image and the results are often unsatisfactory for images with complex phase structures. We have developed a holographic phase imaging method to remove these phase discontinuities by the generation and combination of two phase maps using separate wavelengths[27]. The basic principle of multi-wavelength phase imaging is described by referring to Fig. 2-9, with numerical values that were used in generating the simulation plots. Suppose the object is a tilted plane of height $h = 5.0 \mu\text{m}$. A single-wavelength phase image has 2π discontinuity wherever the height is a multiple of the wavelength. Using wavelengths $\lambda_1 = 0.532 \mu\text{m}$ or $\lambda_2 = 0.633 \mu\text{m}$ the phase map $\varphi_m(x)$, $m = 1$ or 2 , converted to surface profile $z_m(x) = \lambda_m \varphi_m / 2\pi$ will consist of a number of ramps of height equal to the wavelength, Figs. 2-9a) and 2-9b). Subtraction of the two phase maps $\varphi'_{12} = \varphi_1 - \varphi_2$ has numerous discontinuities of 2π , Fig. 2-9c), but adding 2π wherever $\varphi'_{12} < 0$ yields a new phase map $\varphi_{12}(x) = \varphi'_{12} + 2\pi \cdot (\varphi'_{12} < 0)$, with a longer range free of discontinuities. (The parentheses in the last expression is either 1 or 0 depending on whether the inequality is true or false.) In fact the new phase map is equivalent to that of a longer 'beat wavelength' $\Lambda_{12} = \lambda_1 \lambda_2 / |\lambda_1 - \lambda_2| = 3.33 \mu\text{m}$, and the corresponding surface profile is the 'coarse map' $z'_{12}(x) = \Lambda_{12} \varphi_{12}(x) / 2\pi$, Fig. 2-9d). By proper choice of the two wavelengths, the axial range Λ_{12} can be adjusted to any value that would fit the axial size of the object being imaged[28,29,30]. This technique provides a straightforward and efficient phase imaging method in a wide range of applications. A limitation is that any phase noise in each single-wavelength phase map is amplified by a factor equal to the magnification of the wavelengths. The other half of the phase imaging method consists of an algorithm to reduce the noise back to the level of the single-wavelength phase maps. This is accomplished by using the coarse map to determine z within an integer n -multiple of a wavelength, say λ_1 , and pasting the single-wavelength phase map φ_1 to $n\lambda_1$, to obtain the 'fine map'. Figure 2-10 shows perspective views of phase maps of the surface of a resolution target. Figures 2-10a) and 2-10b) are

single-wavelength phase maps using the two wavelengths $\lambda_1 = 0.532 \mu\text{m}$ and $\lambda_2 = 0.633 \mu\text{m}$. Figure 2-10c) is the coarse map and Fig. 2-10d) is the fine map.

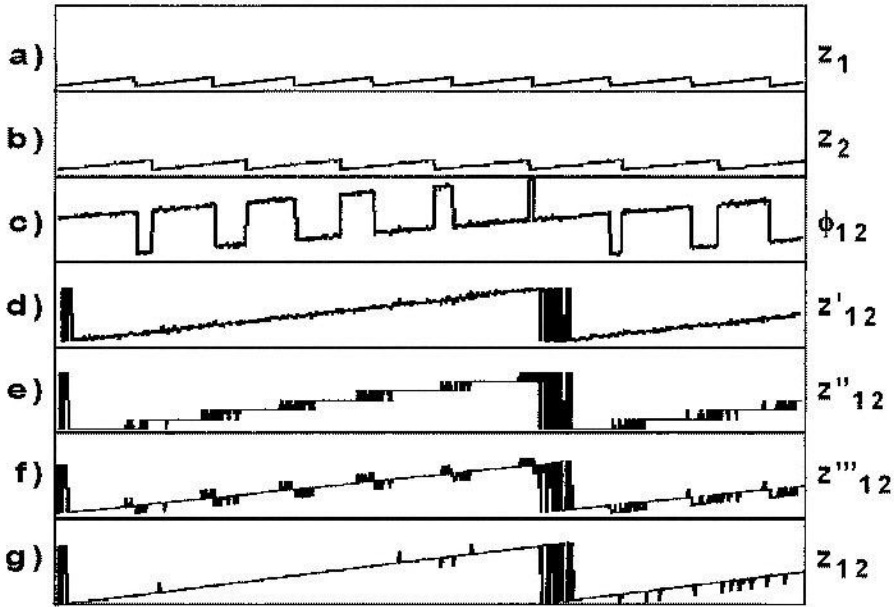


Figure 2-9. Simulation of two-wavelength phase imaging digital holography. a) height profile of a $10 \mu\text{m}$ high incline, derived from phase of $0.532 \mu\text{m}$; b) derived from phase of $0.633 \mu\text{m}$; c) difference phase map ϕ_{12} ; d) coarse map z'_{12} , with beat wavelength $3.33 \mu\text{m}$; e) z''_{12} , where z'_{12} is divided into integer multiples of 2π ; f) z'''_{12} , where z'_{12} is pasted on z''_{12} ; g) fine map, z_{12} , where most of the spikes in z'_{12} are removed by comparison with z''_{12} . The vertical axis is $5.0 \mu\text{m}$ full scale in every panel, except for c) where the vertical range is -2π to $+2\pi$.

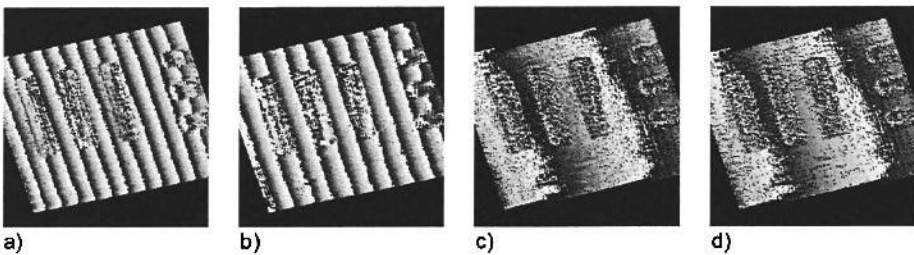


Figure 2-10. Two-dimensional profiles of a resolution target, $157 \times 157 \mu\text{m}^2$ with 360×360 pixels, from two-wavelength phase imaging digital holography. a) phase map $z_1(x, y)$ derived from phase $\phi_1(x, y)$ of $\lambda_1 = 0.532 \mu\text{m}$; b) phase map $z_2(x, y)$ derived from phase $\phi_2(x, y)$ of $\lambda_2 = 0.633 \mu\text{m}$; c) coarse map $z'_{12}(x, y)$; d) fine map $z_{12}(x, y)$.

The method of phase imaging and phase unwrapping works equally well on biological microscopy. In Fig. 2-11, a $193 \times 193 \mu\text{m}^2$ area of a layer of onion cells is imaged. The single wavelength phase images of Figs. 2-11a) and 2-11b) contain numerous 2π discontinuities, making it difficult to discern the cell body and walls. These discontinuities are completely removed in the phase-unwrapped image of Fig. 2-11c), and one can clearly observe the cell bodies delineated by the cell walls. Note, in particular, that conventional phase unwrapping technique, Fig. 2-11d), has difficulty with the quite irregular image of the onion cells shown. Furthermore, the method can be extended to three- or more-wavelength phase imaging to increase the beat wavelength further without introducing amplification of noise.

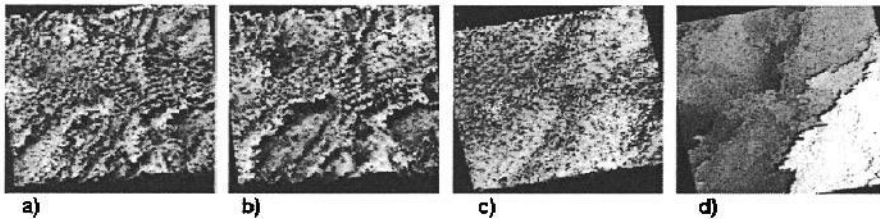


Figure 2-11. Two-dimensional profiles of onion cells, $193 \times 193 \mu\text{m}^2$ with 360×360 pixels, from two-wavelength phase imaging digital holography. a) phase map derived from phase of $0.532 \mu\text{m}$; b) phase map derived from phase of $0.633 \mu\text{m}$; c) fine map; d) unwrapped phase map using numerical algorithm.

5. WAVELENGTH-SCANNING DIGITAL INTERFERENCE HOLOGRAPHY

Although the hologram produces a 3D image of the optical field, this does not by itself yield the topographic or tomographic distance information, other than by focusing and defocusing of the image points. The distance information can be obtained by counting the number of wavelengths or some multiples of it, which is the basis of various interference techniques. A well-known technique is the interference of two holograms recorded at two different wavelengths, resulting in a contour interferogram with the axial distance between the contour planes inversely proportional to the difference in wavelengths, $\Lambda \sim \lambda^2 / \Delta\lambda$. In digital holography, it is possible to extend the process to recording and reconstruction of many holograms without introducing any wavelength mismatch. If a number, N , of regularly spaced wavelengths are used for recording and reconstruction, then the peaks of the

cosine squared intensity variation of the two-wavelength interference become sharper and narrower, $\delta = \Lambda / N$, as when a number of cosines with regularly spaced frequencies are added. We are developing wavelength scanning digital interference holography (WSDIH) as a novel method of microscopic three-dimensional imaging by numerical superposition of a number of holographic fields taken with varying wavelengths[31,32,33]. Unlike some of the other 3D microscopic methods such as confocal microscopy and optical coherence tomography[34], the digital interference holography does not involve pixel-by-pixel mechanical scanning of three-dimensional volume and yet achieves comparable resolutions. Wide field optical coherence tomography is another 3D imaging method using incoherent light interference imaging[35,36].

Suppose an object is illuminated by a laser beam of wavelength λ . A point P (at \mathbf{r}_p) on the object scatters the illumination beam into a Huygens wavelet, $A(\mathbf{r}_p)\exp(ik|\mathbf{r}-\mathbf{r}_p|)$, where $A(\mathbf{r}_p)$ is proportional to the amplitude and phase of the scattered wavelet. For an extended object, the field at \mathbf{r} is

$$E(\mathbf{r}) \sim \int A(\mathbf{r}_p)\exp(ik|\mathbf{r}-\mathbf{r}_p|)d^3\mathbf{r}_p, \quad (2-16)$$

where the integral is over the object volume. The amplitude and phase of this field at the hologram plane $z = 0$ is recorded by the hologram. If the holographic process is repeated using N different wavelengths, and the reconstructed fields are all superposed together, then the resultant field is

$$\begin{aligned} E(\mathbf{r}) &\sim \sum_k \int A(\mathbf{r}_p)\exp(ik|\mathbf{r}-\mathbf{r}_p|)d^3\mathbf{r}_p \sim \int A(\mathbf{r}_p)\delta(\mathbf{r}-\mathbf{r}_p)d^3\mathbf{r}_p \\ &\sim A(\mathbf{r}). \end{aligned} \quad (2-17)$$

That is, for a large enough number of wavelengths, the resultant field is proportional to the field at the object and is nonzero only at the object points. In practice, if one uses a finite number N of wavelengths at regular intervals of $\Delta(1/\lambda)$, then the object image $A(\mathbf{r})$ repeats itself (other than the diffraction/defocusing effect of propagation) at a beat wavelength $\Lambda = [\Delta(1/\lambda)]^{-1}$, with axial resolution $\delta = \Lambda/N$. By use of appropriate values of $\Delta(1/\lambda)$ and N , the beat wavelength Λ can be matched to the axial extent of the object, and δ to the desired level of axial resolution.

In a WSDIH experiment, the wavelength of a dye laser is scanned in the range of 575.0 ~ 605.0 nm in 20 steps, taking the exposure of a hologram at each step. The optical field of a volume around the image location is calculated by numerical diffraction from each hologram. At this point, the

field patterns in the individual 3D arrays show little variation along a few millimeters of z-direction. Now the twenty 3D arrays are numerically superposed together, by adding the arrays elementwise, resulting in the accumulated field array of the same size. This new array then has field distribution that represents the three-dimensional object structure, with axial range of $\Lambda = 220 \mu\text{m}$ and axial resolution of $\delta = 11 \mu\text{m}$, as described above. Figure 2-12 illustrates the building up of axial resolution as a series of holographic images are superposed using a range of wavelengths. The five frames shown are with one, two, four, eight, and twenty wavelengths superposed, and one notices the narrowing of the contour widths as the synthesized coherence length shortens. Figure 2-13 shows a few contour images at $60\mu\text{m}$ axial distance intervals.



Figure 2-12. Build up of axial resolution by superposition of holographic images of a penny using a range of wavelengths with $N = 1, 2, 4, 8$, and 20 .

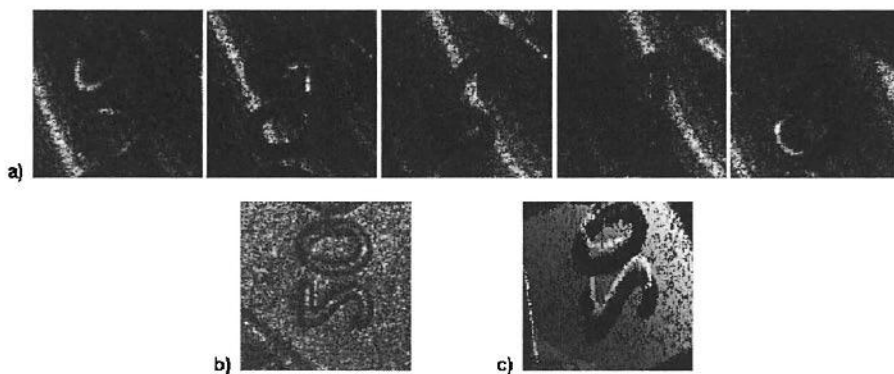


Figure 2-13. a) Contour images at various axial distances in the WSDIH image of a penny. The image volume is $2.62 \text{ mm} \times 2.62 \text{ mm} \times 200 \mu\text{m}$, and $N = 20$, so that . b) Flat view of DIH by adding all the contour images. c) Perspective view of the 3D reconstruction of the penny by WSDIH.

The digital interference holography is a coherent imaging method and is capable of tomographic imaging through a thickness of scattering medium. Figure 2-14 is the result of a DIH imaging experiment on a $2.62 \times 2.62 \text{ mm}^2$ area of a piece of beef tissue. Here we have used wavelengths in the range of $585.0 \sim 591.9 \text{ nm}$ at 41 steps so that the axial range is $\Delta = 2.00 \text{ mm}$ and the axial resolution $\delta = 50 \text{ }\mu\text{m}$. The specimen was a thin layer of beef tissue pressed to about 1.5 mm thickness on a slide glass and otherwise exposed to air. The images in Fig. 2-14(a) show tissue layers at several depths up to about 1.5 mm below surface. Much of the reflection signals are apparently from the tissue-air and tissue-glass interface. One can discern the striation of muscle fiber bundles. Figure 2-14(b) shows variations of the tissue layers in a few x-z cross-sectional images.

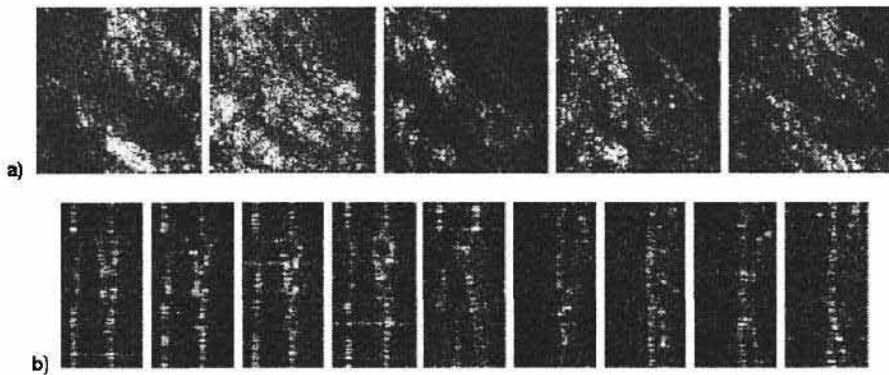


Figure 2-14. WSDIH tomography of a beef tissue. The image volume is $2.62 \text{ mm} \times 2.62 \text{ mm} \times 2.0 \text{ mm}$, and $N = 30$, so that and , a) x-y transverse images at several depths up to 1.5 mm . b) x-z cross-sectional images displaying variations of tissue layers across the field.

6. CONCLUSIONS

In conclusion, we have presented the recent developments of digital holographic techniques for biological microscopy applications. Different numerical reconstruction algorithms are reviewed and compared. As the most frequently used method, the Fresnel theory offers quality reconstruction without aliasing if the reconstruction distance is larger than the minimum object-to-hologram distance. Although the Fresnel diffraction formula can still give an accurate reconstruction for smooth and slowly varying objects where the Fresnel approximation is not strictly satisfied, it cannot correctly reconstruct near wave fields for more diffractive objects,

where the higher-order terms in the expansion of the Fresnel approximation are more significant. The angular spectrum method in contrast, demonstrates flexibility and effectiveness in image reconstruction without the limitation of having to satisfy a minimum object-to-hologram distance as in Fresnel diffraction.

In this paper we have also presented experimental results that demonstrate the capabilities of digital holography for biological microscopy. In holographic movies a series of holograms are recorded and the images are reconstructed with numerically adjustable focus so that the rapidly moving microbes can be accurately tracked. Real-time imaging is possible because only one exposure per time frame is required. The lateral and longitudinal resolutions obtained are consistent with diffraction limited imaging. Digital holography and movies of digital holography therefore are seen to be a useful new tool for biological microscopy.

Although numerical phase unwrapping methods are an established technique, they have difficulty correctly interpreting the phase images of rough and irregular objects. In this paper, we have demonstrated the use of an optical method of phase unwrapping by use of two or more wavelengths in digital holography. Through the application of this technique it is possible to remove 2π ambiguities and increase the axial range. The noise in the final phase profile is that of the single wavelength phase profile. The technique can be applied to incoherent interference imaging as well as holographic imaging.

Finally, we have described the principle of multi-wavelength scanning digital interference holography. By superposition of a number of numerically reconstructed optical diffraction fields of digital holograms that are optically recorded with varying wavelengths, it results in a synthesized short coherence length and corresponding axial resolution. Experimental results are presented to verify the principles.

ACKNOWLEDGEMENT

The authors gratefully acknowledge the financial support for this work by the National Science Foundation.

REFERENCES

- [1] U. Schnars and W.P. Jueptner, "Direct recording of holograms by a CCD target and numerical reconstruction", *Appl. Opt.* **33**, 179-81 (1994).

- [2] S. Grilli, P. Ferraro, S. De Nicola, A. Finizio, G. Pierattini and R. Meucci, "Whole optical wavefields reconstruction by digital holography", *Opt. Express* **9**, 294-302 (2001).
- [3] U. Schnars and W.P.O. Jueptner, "Digital recording and numerical reconstruction of holograms", *Meas. Sci. Technol.* **13**, R85-R101 (2002).
- [4] J.W. Goodman and R.W. Lawrence, "Digital image formation from electronically detected holograms", *Appl. Phys. Lett.* **11**, 77-79 (1967).
- [5] S. Seebacher, W. Osten and W. Jueptner, "Measuring shape and deformation of small objects using digital holography", *Proc. SPIE* **3479**, 104-15 (1998).
- [6] L. Xu, X. Peng, J. Miao and A.K. Asundi, "Studies of digital microscopic holography with applications to microstructure testing", *Appl. Opt.* **40**, 5046-5051 (2001).
- [7] W.S. Haddad, D. Cullen, J.C. Solem, J.W. Longworth, A. McPherson, K. Boyer and C.K. Rhodes, "Fourier-transform holographic microscope", *Appl. Opt.* **31**, 4973-8 (1992).
- [8] D. Dirksen, H. Droste, B. Kemper, H. Delere, M. Deiwick, H.H. Scheld and G. von Bally, "Lensless Fourier holography for digital holographic interferometry on biological samples", *Opt. Lasers Eng.* **36**, 241-249 (2001).
- [9] W. Xu, M.H. Jericho, I.A. Meinertzhagen and H.J. Kreuzer, "Digital in-line holography for biological applications", *Proc. Natl. Acad. Sci. USA* **98**, 11301-05 (2001).
- [10] I. Yamaguchi, J. Kato, S. Ohta and J. Mizuno, "Image formation in phase-shifting digital holography and applications to microscopy", *Appl. Optics* **40**, 6177-6186 (2001).
- [11] U. Schnars, "Direct phase determination in hologram interferometry with use of digitally recorded holograms", *J. Opt. Soc. Am. A* **11**, 2111-5 (1994).
- [12] A. Barty, K.A. Nugent, D. Paganin and A. Roberts, "Quantitative optical phase microscopy", *Opt. Lett.* **23**, 817-9 (1998).
- [13] E. Cuche, F. Bevilacqua and C. Depeursinge, "Digital holography for quantitative phase-contrast imaging", *Opt. Lett.* **24**, 291 (1999).
- [14] E. Cuche, P. Marquet and C. Depeursinge, "Simultaneous amplitude-contrast and quantitative phase-contrast microscopy by numerical reconstruction of Fresnel off-axis holograms", *Appl. Optics* **38**, 6994-7001 (1999).
- [15] P. Ferraro, S. De Nicola, A. Finizio, G. Coppola, S. Grilli, C. Magro and G. Pierattini, "Compensation of the inherent wave front curvature in digital holographic coherent microscopy for quantitative phase-contrast imaging", *Appl. Opt.* **42**, 1938-46 (2003).
- [16] L.F. Yu and L.L. Cai, "Iterative algorithm with a constraint condition for numerical reconstruction of a three-dimensional object from its hologram", *Journal of the Optical Society of America a-Optics Image Science and Vision* **18**, 1033-1045 (2001).
- [17] K. Matsushima, H. Schimmel and F. Wyrowski, "Fast calculation method for optical diffraction on tilted planes by use of the angular spectrum of plane waves", *Journal of the Optical Society of America a-Optics Image Science and Vision* **20**, 1755-1762 (2003).
- [18] W. Osten, T. Baumbach and W. Jueptner, "Comparative digital holography", *Opt. Lett.* **27**, 1764 (2002).
- [19] T.-C. Poon, "Three-dimensional image processing and optical scanning holography", *Adv. Imaging & Electron Phys.* **126**, 329-350 (2003).
- [20] I. Yamaguchi and T. Zhang, "Phase-shifting digital holography", *Opt. Lett.* **22**, 1268 (1997).
- [21] T. Zhang and I. Yamaguchi, "Three-dimensional microscopy with phase-shifting digital holography", *Opt. Lett.* **23**, 1221 (1998).

- [22] M. Jacquot, P. Sandoz and G. Tribillon, "High resolution digital holography", *Opt. Commun.* **190**, 87-94 (2001).
- [23] J.W. Goodman, *Introduction to Fourier Optics, 2nd ed* (New York, McGraw-Hill, 1996).
- [24] C.F. Lo, X. Peng and L.L. Cai, "Surface normal guided method for two-dimensional phase unwrapping", *Optik* **113**, 439-447 (2002).
- [25] M. Servin, J.L. Marroquin, D. Malacara and F.J. Cuevas, "Phase unwrapping with a regularized phase-tracking system", *Appl. Opt.* **37**, 1917-23 (1998).
- [26] M.A. Schofield and Y. Zhu, "Fast phase unwrapping algorithm for interferometric applications", *Opt. Lett.* **28**, 1194 (2003).
- [27] J. Gass, A. Dakoff and M.K. Kim, "Phase imaging without 2-pi ambiguity by multiwavelength digital holography", *Opt. Lett.* **28**, 1141-3 (2003).
- [28] Y.Y. Cheng and J.C. Wyant, "Two-wavelength phase shifting interferometry", *Appl. Opt.* **23**, 4539-43 (1984).
- [29] K. Creath, "Step height measurement using two-wavelength phase-shifting interferometry", *Appl. Opt.* **26**, 2810-6 (1987).
- [30] P. de Groot, "Extending the unambiguous range of two-color interferometers", *Appl. Opt.* **33**, 5948-53 (1994).
- [31] M.K. Kim, "Wavelength scanning digital interference holography for optical section imaging", *Opt. Lett.* **24**, 1693 (1999).
- [32] M.K. Kim, "Tomographic three-dimensional imaging of a biological specimen using wavelength-scanning digital interference holography", *Opt. Express* **7**, 305-10 (2000).
- [33] A. Dakoff, J. Gass and M.K. Kim, "Microscopic three-dimensional imaging by digital interference holography", *J. Electr. Imag.* **12**, 643-647 (2003).
- [34] D. Huang, E.A. Swanson, C.P. Lin, J.S. Schuman, W.G. Stinson, W. Chang, M.R. Hee, T. Flotte, K. Gregory, C.A. Puliafito and J.G. Fujimoto, "Optical coherence tomography", *Science* **254**, 1178-81 (1991).
- [35] A. Dubois, L. Vabre, A.C. Boccara and E. Beaurepaire, "High-resolution full-field optical coherence tomography with Linnik microscope", *Appl. Opt.* **41**, 805-12 (2002).
- [36] L. Yu and M.K. Kim, "Full-color three-dimensional microscopy by wide-field optical coherence tomography", *Opt. Express* **12**, 6632-6641 (2004).

Digital Holography and Three-Dimensional Display
Principles and Applications

Poon, T.-C. (Ed.)

2006, XIV, 430 p., Hardcover

ISBN: 978-0-387-31340-5